Optical Materials 40 (2015) 41–48

Contents lists available at ScienceDirect

Optical Materials

journal homepage: www.elsevier.com/locate/optmat

Low temperature synthesis and optical properties of the R_2O_3:Eu^{3+} nanophosphors (R^{3+}: Y, Gd and Lu) using TMA complexes as precursors

I.G.N. Silva [a], L.C.V. Rodrigues [a,b], E.R. Souza [a], J. Kai [c], M.C.F.C. Felinto [d], J. Hölsä [a,b,e], H.F. Brito [a,*], O.L. Malta [f]

[a] Instituto de Química, Universidade de São Paulo, São Paulo, SP, Brazil
[b] Department of Chemistry, University of Turku, Turku, Finland
[c] Departamento de Química, Pontifícia Universidade Católica do Rio de Janeiro, Rio de Janeiro, RJ, Brazil
[d] Centro de Química e Meio Ambiente, Instituto de Pesquisas Energéticas e Nucleares, São Paulo, SP, Brazil
[e] Turku University Centre for Materials and Surfaces (MatSurf), Turku, Finland
[f] Departamento de Química Fundamental, Universidade Federal de Pernambuco, Recife, PE, Brazil

ARTICLE INFO

Article history:
Received 18 June 2014
Received in revised form 4 November 2014
Accepted 27 November 2014
Available online 24 December 2014

Keywords:
Benzenetricarboxylate precursors
Europium doping
Gadolinium
Yttrium and lutetium sesquioxides
Photoluminescence

ABSTRACT

The R_2O_3:Eu^{3+} (R^{3+}: Y, Gd and Lu) nanophosphors were synthesized with a low temperature thermolysis method using rare earth 1,3,5-benzenetricarboxylate (TMA) complexes as precursors. The R(TMA):Eu^{3+} (1 mole %) complexes were synthesized using the co-precipitation method which complexes were then annealed at temperatures from 500 to 1000 °C for 1 h, yielding the cubic C-type R_2O_3:Eu^{3+} materials. The XPD patterns revealed no impurities in C-R_2O_3 obtained at any temperature. The Scherrer's equation based on powder diffraction data confirmed an increase in crystallite size from 6 to 52 nm with increasing annealing temperature from 500 to 1000 °C for Y_2O_3, respectively, agreeing with the SEM and TEM data. Similar results were obtained for the other R_2O_3:Eu^{3+}. The excitation spectra show a broad oxide to europium charge transfer absorption band at 260 nm, *i.e.* $O^{2-}(2p) \rightarrow Eu^{3+}(4f^6)$ LMCT, as well as the narrow lines assigned to the 4f–4f transitions of the Eu^{3+} ion. The characterization of the photoluminescence properties of the phosphors was also based on the analysis of the emission spectra and luminescence decay curves. The experimental intensity parameters (Ω_λ), lifetimes (τ), as well as radiative (A_{rad}) and non-radiative (A_{nrad}) decay rates were calculated and discussed.

1. Introduction

During the last five decades, luminescent rare earth (R^{3+}) materials have attracted much interest due to their special spectroscopic properties and commercial applications in different areas such as: displays, lighting, lasers, luminescent security inks [1–6]. The Y_2O_3:Eu^{3+} phosphor shows almost monochromatic red emission colour, high emission quantum yield and good thermal stability.

The cubic C-type rare earth sesquioxides C-R_2O_3 can be readily doped with Eu^{3+} ions, which usually exhibit high luminescence efficiency. The Eu^{3+} ions occupy two six-fold coordinated non-equivalent sites with C_2 and S_6 symmetries (Fig. 1) [7]. The induced electric dipole transitions in the S_6 site cannot gain intensity by the mixing of opposite parity electronic configurations with the $4f^N$ one. However, the relatively weak magnetic dipole-induced transitions remain possible for ions in a site with inversion centre. In contrast to the S_6 site, the C_2 site has no centre of inversion that drastically affects the luminescence spectra of the Eu^{3+}-doped materials. For example, the red emission colour of the Eu^{3+} doped cubic C-R_2O_3 is dominated by the hypersensitive $^5D_0 \rightarrow {}^7F_2$ transition of the Eu^{3+} ion in the C_2 site.

In the R_2O_3 lattices, the Eu^{3+} dopant ion can substitute the other R^{3+} ions without introducing major distortions in the crystal structure, owing to the similarity of the ionic radii (in Å) of Eu^{3+} (0.947), Gd^{3+} (0.938), Y^{3+} (0.900) and Lu^{3+} (0.861) [8], following the *Vegard's rule* [9]. Besides, the Eu^{3+} doped R_2O_3 materials usually show an intense absorption band in the ultraviolet region, consistent with the allowed transition: $O^{2-}(2p) \rightarrow Eu^{3+}(4f^6)$ ligand-to-metal charge-transfer states (LMCT), which can improve its luminescence efficiency [10].

With the advent of nanoscience and nanotechnology, the photonic and morphological properties of R_2O_3:Eu^{3+} nanomaterials have been retaken and reinvestigated with new focuses [11,12]. These phosphors have been prepared by sol–gel [12], chemical vapour deposition [13], microemulsion [14,15], spray pyrolysis

* Corresponding author. Tel.: +55 11 30913708; fax: +55 11 38155579.
E-mail address: hefbrito@iq.usp.br (H.F. Brito).

http://dx.doi.org/10.1016/j.optmat.2014.11.044
0925-3467/

[16,17], co-precipitation [18,19], hydrothermal [20] and combustion methods [21].

In this work, R_2O_3:Eu^{3+} nanophosphors (R^{3+}: Y, Gd and Lu) were prepared for the first time with a thermolysis method using R(TMA):Eu^{3+} complexes as precursors. This synthesis method produces highly luminescent nanomaterials by one-step ligand decomposition which occurs at lower temperature than for the solid state method, producing the sesquioxides at around 500 °C [22]. The structure and surface morphology were characterized by thermogravimetric analyses (TG–DTG), infrared absorption spectroscopy (FTIR), X-ray powder diffraction (XPD), scanning electron microscopy (SEM) and transmission electron microscopy (TEM) techniques. The photoluminescence properties were evaluated based on the excitation and emission spectra, as well as luminescence decay lifetimes of the emitting $^5D_0$ level of Eu^{3+}. The experimental intensity parameters, emission efficiency, radiative and non-radiative probabilities and CIE colour coordinates (x,y) were also determined.

2. Experimental

The rare earth chlorides $RCl_3{\cdot}6H_2O$ (R: Y, Gd, Eu and Lu) were prepared from their respective oxides (CSTARM, 99.99%) by digestion of the corresponding aqueous suspensions with the addition of concentrated hydrochloric acid until pH reached *ca.* 6.0. The benzene-1,3,5-tricarboxylic acid (trimesic acid, Fluka, 97%), H_3(TMA), was used without further purification. Aqueous Na_3(TMA) solution was prepared by the drop-wise addition of 1 M sodium hydroxide solution in the aqueous H_3(TMA) suspension up to pH of *ca.* 6.0.

For the preparation of the R(TMA):Eu^{3+} complexes, 50 cm^3 of aqueous RCl_3 solution (0.05 M) was added slowly (*ca.* 1 drop *per* second) into 200 cm^3 of the previously prepared Na_3(TMA) solution (0.0125 M) with a 1:1 molar ratio at *ca.* 100 °C. The reaction mixture was refluxed for 4 h and the precipitate was filtered and washed four times with distilled water, dried and stored at reduced pressure. The R(TMA):Eu^{3+} complexes obtained are non-hygroscopic, white crystalline powders, stable in air and insoluble in solvents such as acetone, ethylalcohol, dimethyl sulfoxide, acetonitrile, chloroform and water. Afterwards, the R_2O_3:Eu^{3+} nanomaterials were obtained by annealing the R(TMA):Eu^{3+} complexes at 500, 600, 700, 800, 900 and 1000 °C temperatures in static air.

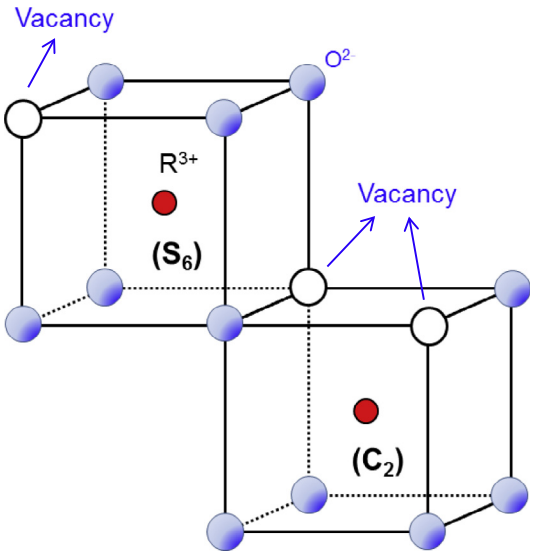

Fig. 1. A schematic illustration of the R^{3+} ions occupying the two six-fold coordinated sites with C_2 and S_6 symmetries in cubic C-R_2O_3 [7].

The elemental analysis of the hydrogen and carbon contents was performed with a Perkin-Elmer CHN 2400 elemental analyser. The infrared absorption spectra were recorded using the KBr pellet technique with a Bomem MB100 FTIR spectrometer in the spectral range from 400 to 4000 cm^{-1}. The XPD patterns were recorded by a Rigaku Miniflex II ($CuK_{\alpha1}$, 1.5406 Å) from 4 to 70° (in 2θ). The TG–DTG analyses were obtained with a TA Instruments HI-RES TGA 2850 equipment in the temperature interval from 30 to 900 °C with constant heating rate of 5 °C min^{-1}, in dynamic synthetic air with a flow rate of 50 cm^3 min^{-1}.

The average crystal size of the materials was estimated from the powder diffraction data by using the Scherrer formula (Eq. (1)) [23] where D is the average crystal size (nm), λ the X-ray wavelength (m), β the full width at half maximum (FWHM) of the selected reflection (rad) and θ (°) half of the Bragg angle (2θ). In the present work, the (222) reflection (2θ: 28.3 °) was used. The reflection broadening due to the diffractometer setup was eliminated from the β_s value (Eq. (2)) by using a microcrystalline sodium chloride reference (β_r) (200 reflection at 32.8°).

$$D = \frac{0.9\lambda}{\beta \cos\theta} \quad (1)$$

$$\beta^2 = \beta_s^2 - \beta_r^2 \quad (2)$$

The SEM images were obtained with a JEOL JSM 7401F Scanning Emission Electron Field Microscope. The solid samples were deposited on a double-sided copper tape, attached to the sample holder. The TEM imaging was performed using a JEM 2100 ARP transmission electron microscope, using an acceleration voltage of 200 kV from a LaB6 thermo-ionic filament yielding 2.4 Å resolution. The images were processed with a Gatan ES500W 35 mm camera (low magnification and SADP images) and Gatan MSC 794 digital camera. Samples were prepared by dispersing the powder in isopropanol. The suspension formed was submitted to ultrasound and was placed on a Cu grid covered with a porous carbon film.

The photoluminescence study was based on the excitation and emission spectra recorded at room temperature (300 K) using front face data collection mode (22.5°), with a 450 W Xenon lamp as the excitation source coupled to a SPEX-Fluorolog 2 spectrometer with 0.22 m double monochromators. The luminescence decay of the phosphors was investigated using the SPEX 1934D phosphorimeter accessory attached with a 150 W pulsed Xenon lamp.

3. Results and discussion

Elemental analysis (H and C) of the chemical compositions of the R(TMA) complexes indicates the 1:1 ratio between the TMA ligand and the R ions (*i.e.* Lu(TMA): calcd: C, 28.29; H, 0.79. found: C, 28.34; H, 0.88%) and the absence of coordinated water molecules in the non-doped R(TMA) complexes (R: Y, Gd and Lu). When the complexes were doped with Eu^{3+} (at 0.1, 0.5, 1 and 5 mole %), the anhydrous complexes were formed, except for the Gd(TMA) doped with 1.0 and 5.0 mole % of Eu^{3+} which contain six coordinated water molecules (Table S1). This result is in agreement with the TG analyses (Fig. 2).

The TG–DTG curves of the non-doped and Eu^{3+} doped complexes were recorded in the temperature interval from 30 to 900 °C. The anhydrous R(TMA) complexes show only one single-step decomposition between 450 and 570 °C (Fig. 2a). On the other hand, the Gd(TMA)·$6H_2O$:Eu^{3+} (1 and 5 mole % of Eu) systems exhibited an additional event, attributed to the removal of six coordinated water molecules (70–150 °C) (Fig. 2b). All the R^{3+} complexes have the final decomposition temperature event higher than 500 °C, but if annealed for 1 h, the respective R_2O_3 sesquioxides are formed (Fig. 2), indicating a kinetic dependence. The decomposition temperature of the R(TMA) complexes varies with

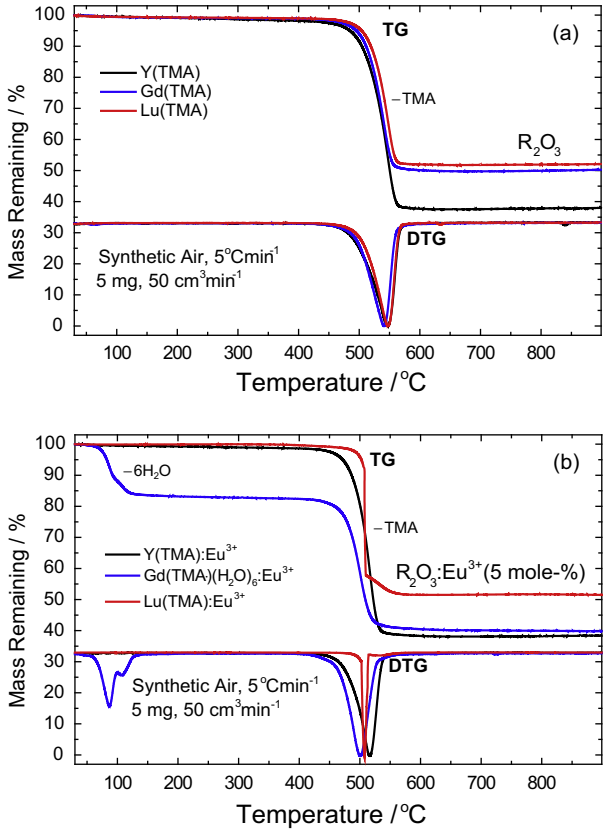

Fig. 2. The TG and DTG curves of (a) R(TMA) and (b) R(TMA):Eu^{3+} (5 mole %) (R: Y, Gd and Lu).

the host cation, decreasing from Y^{3+} to Lu^{3+}. However, the lowest decomposition temperature occurs for the Gd(TMA)·6H_2O:Eu^{3+} (5 mole %) indicating the lower thermal stability of this complex hydrate due to the crystal waters.

The FTIR spectra of the R_2O_3:Eu^{3+} (1 mole %) phosphors annealed at different temperatures (Fig. S1) show a broad absorption band centred at around 3400 cm^{-1} assigned to the O—H stretching vibration mode of the surface hydroxyl groups.

The strength of the OH absorption bands decreases with increasing annealing temperature from 500 to 1000 °C [24,25]. The absorption bands from 1200 to 1750 cm^{-1} are assigned to stretching mode of oxycarbonate arising from the decomposition of the TMA ligand. The C=O absorption decreases with increasing annealing temperature (Fig. S1), due to decomposition of the oxycarbonate [26]. In addition, the absorption bands characteristic of the R^{3+}—O stretching frequencies are centred at 460 and 560 cm^{-1} in the spectra of the annealed samples. The infrared data of the Eu^{3+} doped Y_2O_3, Gd_2O_3 and Lu_2O_3 have similar spectral profiles (Fig. S1).

The XPD patterns (Fig. 3a) show that the R_2O_3:Eu^{3+} materials annealed at 500–1000 °C crystallize in the cubic phase of R_2O_3 with the $Ia\bar{3}$ (a: 10.65 Å, Z: 16) space group [26]. No differences were observed in the 2θ values of the XPD reflections between the materials heated at different temperatures. The absence of impurity reflections indicates that the rare earth sesquioxides are formed with heating at 500 °C for 1 h and that Eu^{3+} substitutes R^{3+} forming a solid solution. The XPD data revealed a complete solid solubility between the Eu^{3+} dopant and the R^{3+} cations in host lattices, due to the similarity between the radius of the Eu^{3+} and other R^{3+} ions [8,9].

The XPD patterns of Y_2O_3:Eu^{3+} (1 mole %) showed broadening of the reflections for the materials annealed at 500 and 600 °C

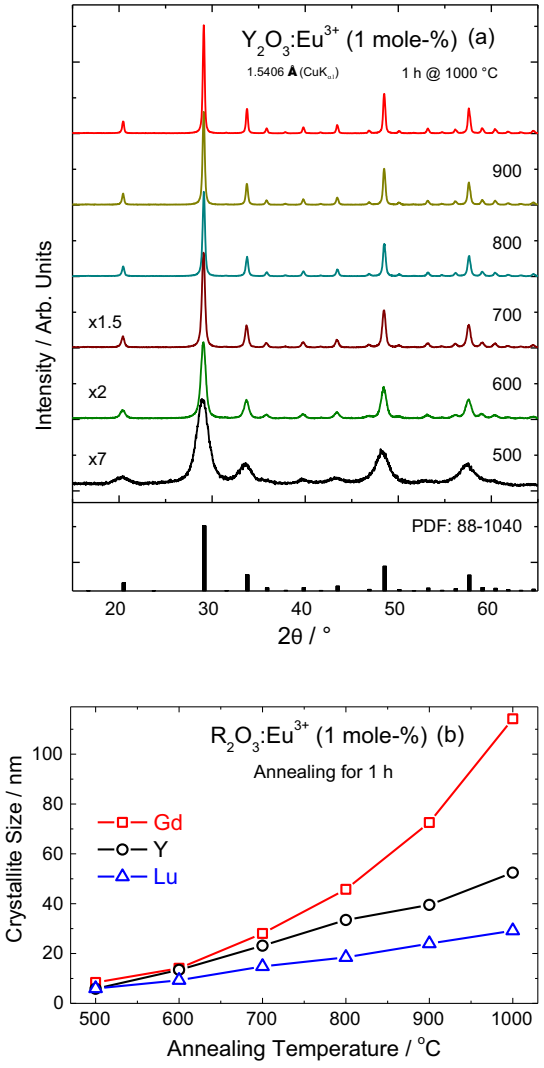

Fig. 3. XPD patterns of Y_2O_3:Eu^{3+} (1 mole %) materials sintered at different temperatures for 1 h (a); PDF: 88-1040 [28] and the correlation between the sesquioxide crystallite size and the annealing temperature for the R_2O_3:Eu^{3+} (1 mole %) materials (b).

(Fig. 3a), indicating smaller crystallite size. The crystallite size increases from 6, 14, 23, 33, 40 and 52 nm with increasing annealing temperature from 500, 600, 700, 800, 900 and 1000 °C, respectively (Fig. 3b), due to sintering of the nanocrystallites favoured at high temperatures. Simultaneously with the enlargement of the crystallite sizes, an increase in crystallinity is also observed at high temperatures as indicated by the higher intensity of the X-ray diffraction reflections.

The XPD data of the Y_2O_3 (Fig. 3a), Gd_2O_3 and Lu_2O_3 (Fig. S2) matrices doped with Eu^{3+} (1 mole %) are very similar. The maximum of the (222) reflection moves to higher 2θ values with the decrease of the ionic radius of the rare earth, in agreement with the Bragg's law [25] and with the decrease in the cubic lattice parameter a. The crystallite size (Fig. 3b) increases in the R_2O_3 with the increasing of R^{3+} radius, as well. The increase can be attributed to the higher reactivity of the Gd_2O_3, with lower melting point (2339 °C) compared with Y_2O_3 (2410) and Lu_2O_3 (2427) [27]. Therefore, the sintering process is favoured for the gadolinium matrix due to the dependence of the partial melting of the nanocrystals. The crystallite size growths can also be explained by the lower decomposition temperature of the Gd precursor (Fig. 2), resulting in a longer sintering time.

The SEM image of the Y(TMA):Eu^{3+} (1 mole %) precursor complex (Fig. 4a) shows that the sheet-like morphology of the complex is similar to the Y_2O_3:Eu^{3+} material after the heat treatment (Fig. 4b), even after annealing at 1000 °C. The oxides exhibited higher porosity due to the decomposition of the organic moiety. This shape property is important to the design of nanomaterials with controlled structure, since it is possible to modify the complex morphology with different synthetic methods and reaction conditions, which would result in the formation of the desired oxide particle shapes. The particle sizes observed in the SEM image of the materials annealed at 1000 °C (Fig. S3) range from 50 to 90 nm.

The TEM images (Fig. 5) confirm the increase in the crystallite size with increasing annealing temperature (Fig. 5a and c). The average particle size estimated from TEM images for Y_2O_3:Eu^{3+} (1 mole %) prepared at temperatures from 500 to 1000 °C ranged from 5 to 52 nm, corroborating well with the Scherrer data. These images also show the cubic shape of the crystals and their narrow size distribution. The particles are agglomerated due to the sheet format of the precursor complexes, however.

At higher magnification (Fig. 5b and d), no defects are observed in the crystals (except for the edges), suggesting the formation of a solid solution between the Eu^{3+} ions and the host matrices. This behaviour is due to the compatibility between the identical trivalent charges and similar ionic radii of the Eu^{3+} dopant ion and the Gd, Y and Lu trivalent host ions of the matrices.

3.1. Analysis of excitation spectra

The excitation spectra of the R_2O_3:Eu^{3+} phosphors (R^{3+}: Y, Gd and Lu) annealed at temperatures from 500 to 1000 °C (Figs. 6 and S4) were recorded in the spectral range from 200 to 590 nm, at room temperature (300 K), with emission monitored at 613 nm. In general, the spectra show the narrow absorption bands of the 4f–4f intraconfigurational transitions originating from the Eu^{3+} ion in the range from 17,000 to 34,000 cm^{-1}. In addition, at higher energy, a broad absorption band can be observed centred at *ca.* 38,900 cm^{-1}, assigned to the $O^{2-}(2p) \rightarrow Eu^{3+}(4f^6)$ ligand to metal charge transfer (LMCT) transition. All excitation spectra exhibit similar spectral features, except for the Gd_2O_3:Eu^{3+} materials the spectra of which also include sharp lines from the 4f–4f intraconfigurational transitions of the Gd^{3+} ion (Figs. 6b and S4b).

The weak $^7F_0 \rightarrow {}^5D_0$ and $^7F_1 \rightarrow {}^5D_0$ (hot bands from the lower $^7F_1$ levels at *ca.* 210 and 280 cm^{-1}) transitions, show only one strong line each at 17,216 and 17,010 cm^{-1} for Y_2O_3:Eu^{3+}, respectively. For more detailed ^7F_J energy level schemes, see the analysis of the Eu^{3+} emission spectra in the next section. The thermal population of the highest $^7F_1$ level at *ca.* 445 cm^{-1} (and the $^7F_2$ levels at *ca.* 1000 cm^{-1}) are quite low but the hot band absorption from these levels can be seen at 300 K as broad bands without enough resolution for exact assignment to be made for $^7F_2$. The transitions observed have similar intensities for all R_2O_3:Eu^{3+} materials annealed at 700 °C (Fig. 6b).

Since the magnetic-dipole induced $^7F_{0,1} \rightarrow {}^5D_1$ transitions of Eu^{3+} are allowed by parity for both the C_2 and S_6 symmetries, several narrow absorption lines (or groups of lines) can be observed below 19,050 (C_2) and at 18,990 and 19,120 cm^{-1} (S_6 site), as well. Because of the high intensity of the $^7F_1 \rightarrow {}^5D_1$ transitions they dominate this spectral range, but even hot band excitation from the $^7F_2$ levels can be found – though very weak. The assignment of these energies is in qualitative agreement with those reported in the literature for Lu_2O_3:Eu^{3+} [29,30]. Since the total splitting of the $^7F_1$ level is some 396 cm^{-1} (cf. next section), the expected splitting of the $^5D_1$ levels is some 20–30% of the $^7F_1$ value, *i.e. ca.* 80–130 cm^{-1}. This relation is quite universal among the Eu^{3+} energy levels in different hosts [31] and was observed here for both the C_2 and S_6 sites.

In comparison with other 4f transitions, the absorption bands observed in the spectral region from 21,400 to 21,600 cm^{-1} are prominent and are assigned to the $^7F_0 \rightarrow {}^5D_2$ transition of Eu^{3+}, which is characteristic of the Eu^{3+} doped R_2O_3 excitation spectra (Figs. 6 and S4). In addition, the forbidden $^7F_0 \rightarrow {}^5D_3$ electric-dipole transition can be also observed as three weak absorption lines at 24,300, 24,426 and 24,533 cm^{-1} due to the J-mixing effects in the ^7F_J manifold. Besides, eight narrow bands originating from the $^7F_0 \rightarrow {}^5L_6$ transition are also shown in the spectral range from 24,600 to 25,600 cm^{-1} (Figs. 6 and S4). Other characteristic Eu^{3+} lines, originating from the absorption from the $^7F_{0,1}$ levels to the following ones (energy in cm^{-1}): $^5G_{2-6}$ (25,800), $^5L_{7,8}$ (26,600), $^5D_4$ (27,250–27,800), $^5H_{J'}$, $^5F_{J'}$, $^5I_{J'}$ and $^3P_0$ (29,600–35,150) are also observed.

The excitation spectra of the Gd_2O_3:Eu^{3+} materials are similar to those of Y^{3+} and Lu^{3+} hosts, except for the spectral range at higher energy between 31,600 and 37,000 cm^{-1} (Figs. 6b and S4b). The characteristic $^8S_{7/2} \rightarrow {}^6P_{7/2}$ (*ca.* 31,970 cm^{-1}), $^8S_{7/2} \rightarrow {}^6P_{5/2}$ (*ca.* 32,530 cm^{-1}) and $^8S_{7/2} \rightarrow {}^6P_{3/2}$ (*ca.* 33,100 cm^{-1}) transitions arising from the Gd^{3+} ion resulted in strong absorption lines, indicating energy transfer from the Gd^{3+} to Eu^{3+} ion [32]. The $^8S_{7/2} \rightarrow {}^6I_{7/2}$ (*ca.* 35660 cm^{-1}) and $^8S_{7/2} \rightarrow {}^6I_{9/2}$, $^6I_{17/2}$ (36,000–36,500 cm^{-1}) transitions overlap with the LMCT band [33].

The broad absorption bands are assigned to the $O^{2-}(2p) \rightarrow Eu^{3+}(4f^6)$ LMCT in the R_2O_3:Eu^{3+} phosphors (Figs. 6 and S4). The barycentre values of the LMCT states are 37,930, 38,600 and 38,765 cm^{-1} for the Gd^{3+}, Y^{3+} and Lu^{3+} oxides, respectively. The shifts to higher energy of LMCT bands suggest that the chemical environment of the Lu_2O_3 host lattice exert stronger influence on

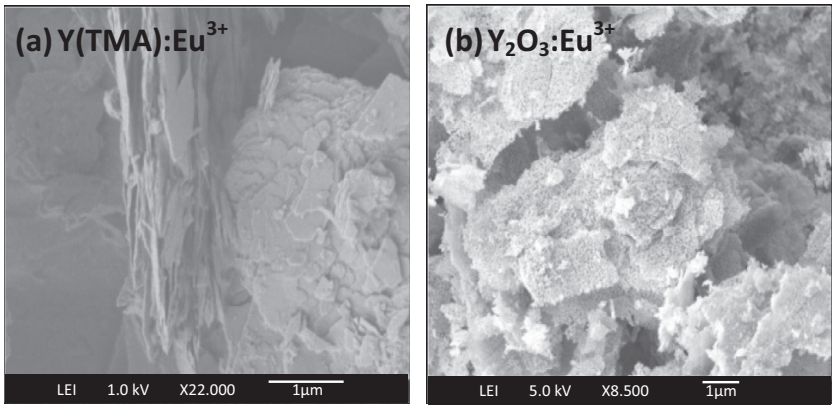

Fig. 4. SEM images of the Y(TMA):Eu^{3+} (1 mole %) complex precursor (a) and Y_2O_3:Eu^{3+} (1 mole %) phosphor sintered for 1 h at 1000 °C (b).

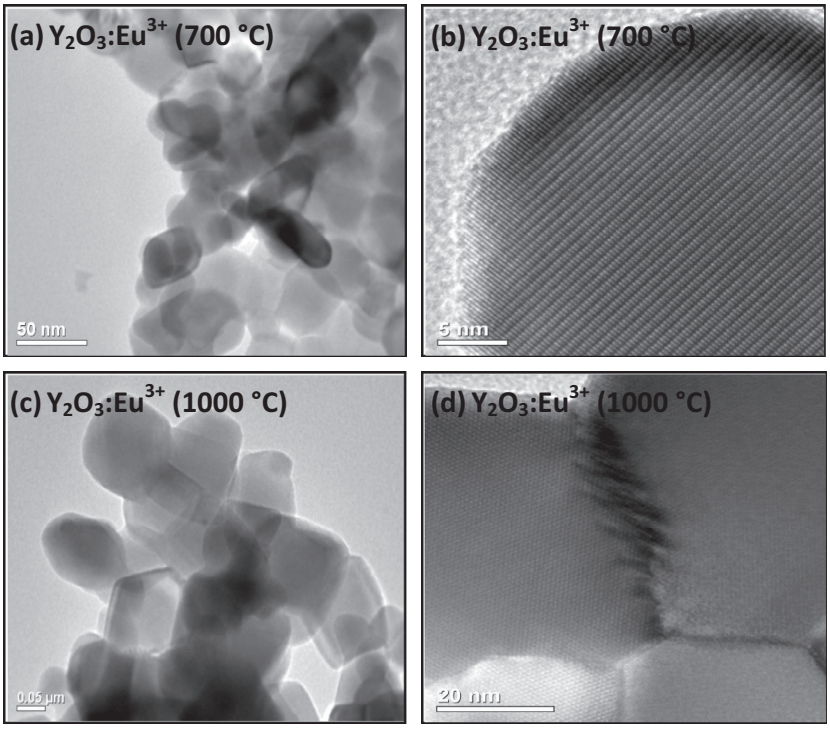

Fig. 5. TEM images of the Y_2O_3:Eu^{3+} (1 mole %) phosphor annealed for 1 h at 700 (a and b) and 1000 °C (c and d).

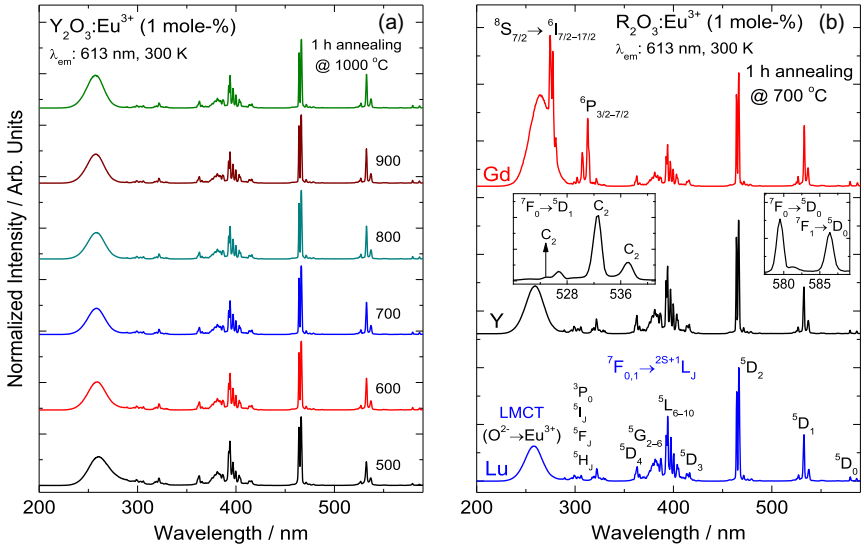

Fig. 6. Excitation spectra recorded at 300 K monitoring the emission at 613 nm of Y_2O_3:Eu^{3+} (1 mole %) annealed at different temperatures (a) and of the R_2O_3:Eu^{3+} (R: Y, Gd and Lu; 1 mole %) oxides annealed at 700 °C (b).

the Eu^{3+} ion than the Gd_2O_3 and Y_2O_3 hosts, due to the decreasing ionic radii [8], the ligand field around the Eu^{3+} ion should be the strongest for the Lu_2O_3 host.

3.2. Analysis of emission spectra

The emission spectra of the R_2O_3:Eu^{3+} phosphors annealed at temperatures from 500 to 1000 °C were recorded in the spectral range from 400 to 850 nm at 300 K, under excitation in the LMCT band at 260 nm (Figs. 7 and S5). All the spectra exhibit narrow emission lines arising from the $^5D_J \rightarrow {}^7F_{J'}$ transitions (J: 0–3 and J′: 0–6) with similar spectral features irrespective of the host; even the material heated at 500 °C shows similar photoluminescent characteristics.

For the materials heated at 700 °C (Fig. 7b), only one emission line at 17,215 cm^{-1} is observed and assigned to the $^5D_0 \rightarrow {}^7F_0$ transition of the Eu^{3+} ion in the C_2 site of the cubic C-type Y_2O_3:Eu^{3+}. The $^5D_0 \rightarrow {}^7F_0$ transition lines broaden with decreasing crystallite size and crystallinity as a result of inhomogeneous broadening. Since the magnetic dipole $^5D_0 \rightarrow {}^7F_1$ transition is allowed for both the C_2 and S_6 sites there are emission lines (Fig. 7b) at 16,666, 16,846 and 17,015 cm^{-1} as well as at 16,770 and 17,165 cm^{-1} originating from the C_2 and S_6 sites, respectively, in fair agreement with [29,30]. Taken into account the splitting of the $^5D_1$ level for

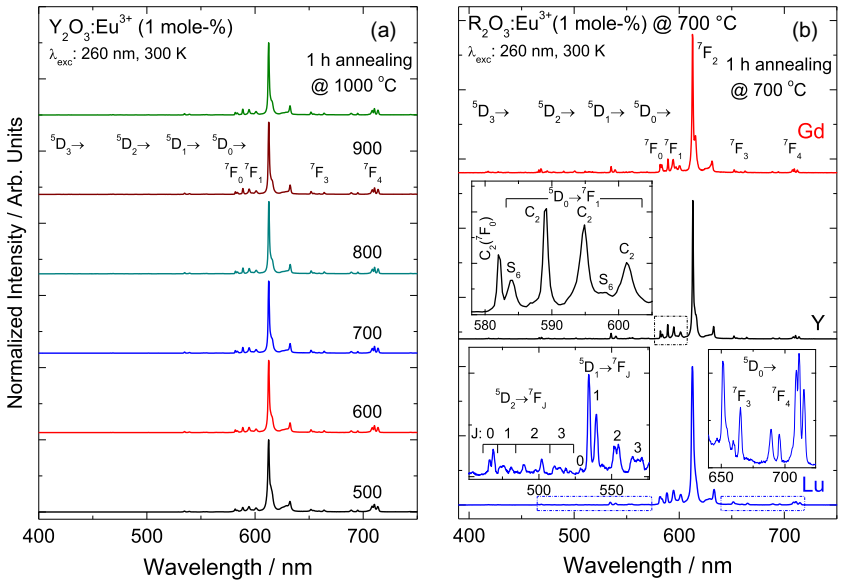

Fig. 7. Emission spectra recorded at 300 K with excitation at 260 nm of Y_2O_3:Eu^{3+} (1 mole %) annealed at different temperatures (a) and of the R_2O_3:Eu^{3+} (R: Y, Gd and Lu; 1 mole %) oxides annealed at 700 °C (b).

the S_6 site, with the $^7F_1$ splitting at *ca.* 400 cm^{-1}, this should be of the order of 80–132 cm^{-1} [31] to which the experimental value (130 cm^{-1}) compares very well. The total $^7F_1$ splittings are 349 and 396 cm^{-1} for the C_2 and S_6 sites, respectively, indicating clearly stronger crystal field effect in the S_6 site. However, the debate over the ^7F_J energy level scheme of Eu^{3+} in C-Y_2O_3 is far from over since the $^7F_1$ barycentre for the S_6 site (330 cm^{-1}) is far too low for such a strong crystal field.

The experimental intensity parameters (Ω_λ) were calculated from the coefficients of spontaneous emission, $A_{0\lambda}$, given by the Eq. (3) [34]:

$$A_{0\lambda} = \frac{4e^2\omega^3}{3hc^3}\chi\sum_y \Omega_\lambda \langle {}^7F_J \| U^{(\lambda)} \| {}^5D_0 \rangle^2 \quad (3)$$

where χ is the Lorentz local field correction term, given by $\chi = [n(n^2+2)^2]/9$, ω the energy of the $^5D_0 \rightarrow {}^7F_J$ transitions and $\langle {}^7F_\lambda \| U^{(\lambda)} \| {}^5D_0 \rangle^2$ the squared reduced matrix elements whose values are 0.0032 and 0.0023 for the $^5D_0 \rightarrow {}^7F_2$ and $^5D_0 \rightarrow {}^7F_4$ transitions, respectively [35].

The refractive index (n) of the bulk R_2O_3:Eu^{3+} is considerably high (~1.9), and in this bulk material the $^5D_0$ lifetime (τ) is around 1.0 ms [36,37]. It is conceivable that in the nanoparticle scale, with average sizes around 20 nm, which are much smaller than the wavelength of the exciting radiation, the n and τ values in the R_2O_3 hosts are different. Moreover, the differences between the Eu^{3+} ions on the surface and within the nanoparticles may play a role in the profile of the decay curves.

The radiative rate (A_{01}) of the $^5D_0 \rightarrow {}^7F_1$ transition of Eu^{3+} ion (allowed by the magnetic dipole interaction) is formally insensitive to the ligand field environment. Therefore it can be used as a reference transition, and has been given values around 50 s^{-1} [38]. Based on this value, the refractive indices were determined and compared to the lifetime and crystallite size values reported in references [36–38]. Both the experimental intensity parameters and measured lifetimes (1.4–2.0 ms) were actually then reproduced using the effective refractive index values between 1.5 and 1.6.

The $A_{0\lambda}$ transition rate values were thus taken as the reference, once it is magnetic dipole allowed and it is also practically independent of the ligand field. The following expression (Eq. (4)) was used [39]:

$$A_{0\lambda} = A_{01}\left(\frac{S_{0\lambda}}{S_{01}}\right)\left(\frac{\omega_{01}}{\omega_{0\lambda}}\right) \quad (4)$$

where S_{01} and $S_{0\lambda}$ are the integrated areas of the $^5D_0 \rightarrow {}^7F_1$ and $^5D_0 \rightarrow {}^7F_\lambda$ transitions, with ω_{01} and $\omega_{0\lambda}$ being their energy barycentres, respectively [37]. Furthermore, the emission quantum efficiency (η) of the $^5D_0$ emitting level of the Eu^{3+} ion was determined according to Eq. (5):

$$\eta = \frac{A_{rad}}{A_{rad} + A_{nrad}} \quad (5)$$

The total decay rate, $A_{tot} = 1/\tau = A_{rad} + A_{nrad}$, where A_{rad} ($= \sum A_{0\rightarrow J}$) and A_{nrad} are the radiative and non-radiative rates of the $^5D_0$ level, respectively.

The values of the experimental intensity parameters (Ω_λ) as well as the radiative (A_{rad}) and non-radiative (A_{nrad}) rates and emission quantum efficiencies (η) of the $^5D_0$ emitting level of the R_2O_3:Eu^{3+} are presented in Table 1. The Ω_2 values are very similar for the same matrix annealed at different temperatures indicating that for each matrix there is no change in the hypersensitive character of the $^5D_0 \rightarrow {}^7F_2$ transition of the Eu^{3+} ion. Therefore, the same chemical environment around Eu^{3+} ion is expected for these materials.

In addition, the emission spectra (Fig. 7) exhibit similar spectral features, corroborating with the similarity of the Ω_2 and Ω_4 values for all matrices.

The considerably high values of the Ω_2 parameters are consistent with a very low point symmetry of the C_2 site occupied by the Eu^{3+} ion. The Eu^{3+} doped Y_2O_3 showed higher values of emission quantum efficiency (η_{aver} = 86%) than Gd_2O_3:Eu^{3+} and Lu_2O_3:-Eu^{3+} (76% and 72%, respectively). The Y_2O_3:Eu^{3+} material annealed at 900 °C also gave the highest value of η = 91% while the Gd_2O_3:-Eu^{3+} at 1000 °C showed the lowest value (η = 65%), due to its high value of the non-radiative rate (A_{nrad} = 246 s^{-1}).

The increase of the annealing temperature improved the quantum efficiency up to 800 °C in all systems, Beyond this temperature, the values stabilize or are lowered probably due to increase in the crystallite size of the R_2O_3:Eu^{3+} materials, especially for Gd_2O_3:Eu^{3+} that has the largest crystallite size, decreasing the emission quantum efficiency.

Table 1
Experimental values of intensity parameters (Ω_λ), radiative (A_{rad}) and non-radiative (A_{nrad}) rates as well as emission lifetimes and emission quantum efficiencies of the $^5D_0$ emitting level determined for the R_2O_3:Eu^{3+} (1 mole%) (R: Y, Gd and Lu) phosphors based on the emission spectra recorded at room temperature.

R_2O_3:Eu^{3+} (1 mole%)	Ω_2 (10^{-20} cm^2)	Ω_4 (10^{-20} cm^2)	A_{rad} (s^{-1})	A_{nrad} (s^{-1})	A_{tot} (s^{-1})	τ (ms)	η (%)
Gd_2O_3:Eu^{3+}							
500 °C	15.1	2.9	541	163	704	1.42	77
600 °C	15.0	1.8	524	145	669	1.49	78
700 °C	13.6	1.3	476	225	701	1.43	68
800 °C	14.4	1.5	503	98	602	1.66	84
900 °C	14.0	1.5	489	107	596	1.68	82
1000 °C	13.2	1.4	465	246	711	1.40	65
Y_2O_3:Eu^{3+}							
500 °C	12.8	1.8	458	104	562	1.78	81
600 °C	13.1	1.6	465	90	554	1.80	84
700 °C	12.8	1.5	454	81	536	1.87	85
800 °C	12.0	1.0	479	52	531	1.88	90
900 °C	13.5	1.3	513	50	563	1.77	91
1000 °C	12.1	1.5	573	84	579	1.72	85
Lu_2O_3:Eu^{3+}							
500 °C	12.5	1.7	449	222	672	1.49	67
600 °C	13.2	1.7	468	200	669	1.49	70
700 °C	12.9	1.6	461	236	697	1.43	66
800 °C	12.6	1.6	419	149	568	1.76	74
900 °C	11.6	1.5	389	120	509	1.96	76
1000 °C	11.5	1.4	383	108	491	2.03	78

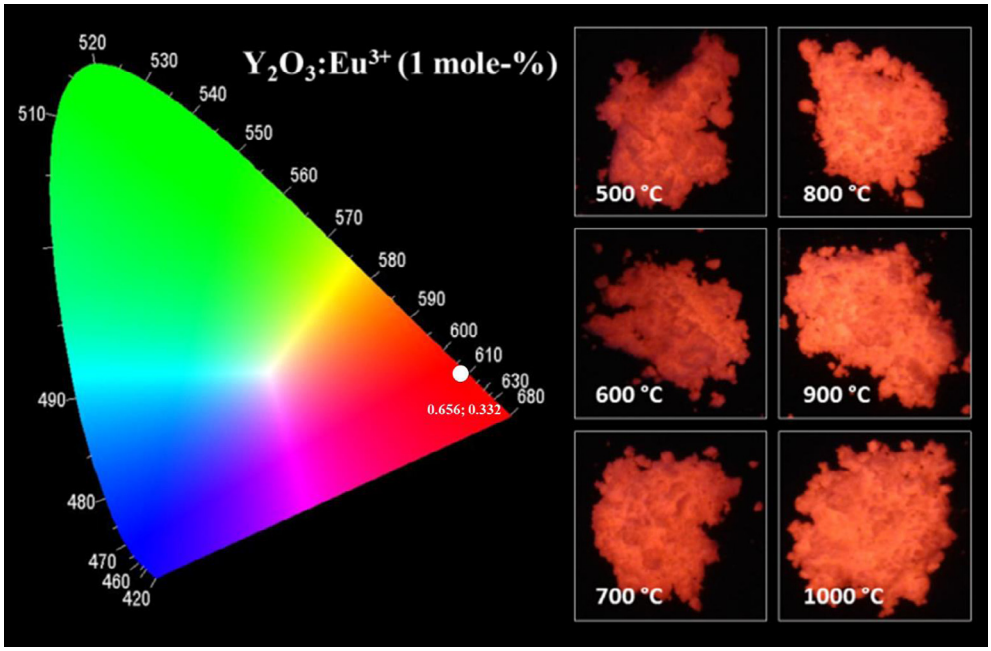

Fig. 8. CIE chromaticity diagram showing the *x*, *y* emission colour coordinates for the R_2O_3:Eu^{3+} (1 mole%) nanophosphors (R: Gd, Y and Lu) annealed at different temperatures. The inset figures are photographs of the Y_2O_3:Eu^{3+} (1 mole%) nanomaterials taken with a digital camera displaying the red emission under UV irradiation at 254 nm. (For interpretation of the references to colour in this figure legend, the reader is referred to the web version of this article.)

The CIE (*Commission Internationale de l'Eclairage*) chromaticity coordinates generated from the emission spectra of Eu^{3+} doped R_2O_3 (Fig. 8) are *x*: 0.656 and *y*: 0.332 [40]. The colour coordinates are practically the same irrespective of the sesquioxide host or the annealing temperature.

The phosphors containing Gd^{3+}, Y^{3+}, Lu^{3+} ions exhibit the same characteristic nearly monochromatic emission. The images of the Y_2O_3:Eu^{3+} (1 mole %) nanomaterials under UV irradiation (inset of Fig. 8) show nearly identical strong red emission for all the phosphors annealed at temperatures from 500 to 1000 °C.

4. Conclusions

R_2O_3:Eu^{3+} nanomaterials were successfully synthesized with an unprecedented method using benzenetricarboxylate precursor complexes annealed at different temperatures, with controllable particle size and high chemical homogeneity. Another advantage of this new synthesis is the significantly lower temperature regime than the usual solid-state method. The TEM and XPD data of the Y_2O_3:Eu^{3+} nanophosphors confirmed the increasing crystallite size with temperature.

The photoluminescence results are consistent with the low symmetry of the C_2 site occupied by the Eu^{3+} ion in the cubic C-type R_2O_3:Eu^{3+}, which is essential for optical applications. Furthermore, the Y_2O_3:Eu^{3+} nanophosphors exhibit high values of emission quantum efficiency, compatible with the commercial phosphors currently available in the market.

Acknowledgements

Financial support is gratefully acknowledged from the Conselho Nacional de Desenvolvimento Científico e Tecnológico (CNPq) and the Academy of Finland through the Brazil–Finland Bilateral Project in the Photonics Program, the Coordenação de Aperfeiçoamento de Pessoal de Nível Superior (CAPES), the Fundação de Amparo à Pesquisa do Estado de São Paulo (FAPESP), Nanobiotec-Brasil – RH-INAMI and inct-INAMI. The authors thank the Laboratório Nacional de Luz Síncrotron (CNPEM/LNLS-C2Nano) for the transmission electron microscopy measurements.

Appendix A. Supplementary material

Supplementary data associated with this article can be found, in the online version, at http://dx.doi.org/10.1016/j.optmat.2014.11.044.

References

[1] G. Blasse, B.C. Grabmeier, Luminescent Materials, Springer Verlag, Berlin, 1994.
[2] C. Feldmann, T. Jüstel, C.R. Ronda, P.J. Schmidt, Adv. Funct. Mater. 13 (2003) 511–516.
[3] K. Marinkovic, L. Mancic, L.S. Gomez, M.E. Rabanal, M. Dramicanin, O. Milosevic, Opt. Mater. 32 (2010) 1606–1611.
[4] A.J. Nelson, E.L. Brant, M.J. Wagner, Chem. Mater. 15 (2003) 688–693.
[5] B.K. Gupta, D. Haranath, S. Saini, V.N. Singh, V. Shanker, Nanotechnology 21 (2010) 055607.
[6] B. Antic, J. Rogan, A. Kremenovic, A.S. Nikolic, M. Vucinic-Vasic, D.K. Bozanic, G.F. Goya, P.H. Colomban, Nanotechnology 21 (2010) 245702.
[7] E. Antic-Fidancev, J. Hölsä, M. Lastusaari, J. Phys.: Condens. Matter 15 (2003) 863–876.
[8] R.D. Shannon, Acta Cryst. A32 (1976) 751–767.
[9] L. Vegard, Z. Phys. 5 (1921) 17–26.
[10] C.Y. Shang, X.Q. Wang, H. Kang, D.M. Han, J. Appl. Phys. 109 (2011) 104309.
[11] X. Ye, W. Zhuang, Y. Hu, T. He, X. Huang, C. Liao, S. Zhong, Z. Xu, H. Nie, G. Deng, J. Appl. Phys. 105 (2009) 064302.
[12] L. Li, H.K. Yang, B.K. Moon, B.C. Choi, J.H. Jeong, K.H. Kim, Mater. Chem. Phys. 119 (2010) 471–477.
[13] B.M. Tissue, H.B. Yuan, J. Solid State Chem. 171 (2003) 12–18.
[14] H. Huang, G.Q. Xu, W.S. Chin, L.M. Gan, C.H. Chew, Nanotechnology 13 (2002) 318–323.
[15] T. Hirai, T. Hirano, I. Komasawa, J. Mater. Chem. 10 (2000) 2306–2310.
[16] K.Y. Jung, K.H. Han, Electrochem. Solid-State Lett. 8 (2005) H17–H20.
[17] H. Saitoh, K. Kawahara, S. Ohshio, A. Nakamura, N. Nambu, Sci. Technol. Adv. Mater. 6 (2005) 205–209.
[18] Y. Sun, L. Qi, M. Lee, B.I. Lee, W.D. Samuels, G.J. Exarhos, J. Lumin. 109 (2004) 85–91.
[19] J. Silver, T.G. Ireland, R. Withnall, J. Electrochem. Soc. 151 (2004) H66–H68.
[20] J.X. Wan, Z.H. Wang, X.Y. Chen, L. Mu, Y.T. Qian, J. Cryst. Growth 284 (2005) 538–543.
[21] O.A. Graeve, S. Varma, G. Rojas-George, D.R. Brown, E.A. Lopez, J. Am. Ceram. Soc. 89 (2006) 926–931.
[22] E.R. Souza, I.G.N. Silva, E.E.S. Teotonio, M.C.F.C. Felinto, H.F. Brito, J. Lumin. 130 (2010) 283–291.
[23] H.P. Klug, L.E. Alexander, X-ray Powder Diffraction Procedures, Wiley, New York, 1959.
[24] M.K. Devaraju, S. Yin, T. Sato, J. Cryst. Growth 311 (2009) 580–584.
[25] M.R. Davolos, S. Feliciano, A.M. Pires, R.F.C. Marques, M. Jafelicci Jr., J. Solid State Chem. 17 (2003) 268–272.
[26] J. Hölsä, T. Turkki, Thermochim. Acta 190 (1991) 335–343.
[27] G. Adachi, N. Imanaka, Chem. Rev. 98 (1998) 1479–1514.
[28] Joint Committee on Powder Diffraction Standards – JCPDS, The International Centre for Diffraction Data – ICDD: Entries 88-1040 (Y_2O_3), 86-2477 (Gd_2O_3) and 86-2475 (Lu_2O_3).
[29] E. Zych, M. Karbowiak, K. Domagala, S. Hubert, J. Alloys Compd. 341 (2002) 381–384.
[30] M. Karbowiak, E. Zych, J. Hölsä, J. Phys.: Condens. Matter 15 (2003) 2169–2181.
[31] B.R. Judd, Operator Techniques in Atomic Spectroscopy, Princeton University Press, Princeton, NJ, USA, 1998. pp. 214–216.
[32] M. Buijs, A. Meyerink, G. Blasse, J. Lumin. 37 (1987) 9–20.
[33] A.G. Macedo, R.A.S. Ferreira, D. Ananias, M.S. Reis, V.S. Amaral, L.D. Carlos, J. Rocha, Adv. Funct. Mater. 20 (2010) 624–634.
[34] C.A. Kodaira, H.F. Brito, O.L. Malta, O.A. Serra, J. Lumin. 101 (2003) 11–21.
[35] W.T. Carnall, H. Crosswhile, Energy Levels Structure and Transition Probabilities of the Trivalent Lanthanides in LaF_3, Argonne National Laboratory, USA, 1977.
[36] J.C. Boyer, F. Vetrone, J.A. Capobianco, A. Speghini, M. Bettinelli, J. Phys. Chem. B 108 (2004) 20137–20143.
[37] R.S. Meltzer, S.P. Feofilov, B. Tissue, H.B. Yuan, Phys. Rev. B 60 (1999) R14012–R14015.
[38] R.M.K. Whiffen, Z. Antic, A. Speghini, M.G. Brik, B. Bártová, M. Bettinelli, M.D. Dramicanin, Opt. Mater. 36 (2014) 1083–1091.
[39] G.F. de Sá, O.L. Malta, C.M. Donega, A.M. Simas, R.L. Longo, P.A. Santa-Cruz, E.F. Silva Jr., Coord. Chem. Rev. 196 (2000) 165–195.
[40] P.A. Santa-Cruz, F.S. Teles, Spectra Lux Software v. 2.0 Beta, Ponto Quântico Nanodispositivos, RENAMI, 2003.